THE JOURNAL OF PHYSICAL CHEMISTRY C
A JOURNAL OF THE AMERICAN CHEMICAL SOCIETY

Plasmon-Induced Electron Transfer between Gold Nanorods and a Carbon Thin Film

Published as part of The Journal of Physical Chemistry C virtual special issue "Hot Electrons in Catalysis".

Tamie Vo and Wei-Shun Chang*

Cite This: *J. Phys. Chem. C* 2024, 128, 321−329 Read Online

ABSTRACT: Plasmonic nanostructures have been demonstrated as emergent photocatalysts because of their efficient photon absorption and their ability to produce hot carriers. However, the plasmon-generated hot carriers decay through ultrafast relaxation pathways, resulting in a short lifetime that impedes the exploitation of hot carriers for chemical reactions. Charge separation at the heterojunction of the hybrid nanostructures can counteract the ultrafast decay to extend the carrier lifetime. Here, we fabricate hybrid nanostructures composed of gold nanorods and a carbon thin film and demonstrate efficient charge transfer between these two materials. Using single-particle dark-field scattering spectroscopy, we observe a broadening of the longitudinal plasmon for gold nanorods on a carbon film compared to those on a glass substrate. We attribute this plasmon damping to the electron transfer from gold nanorods to the carbon film and exclude the contribution from plasmon-induced resonance energy transfer. The electron transfer efficiencies are calculated as 52.8 ± 4.8 and 57.4 ± 4.0% for carbon films with thicknesses of 10 and 25 nm, respectively. This work demonstrates efficient charge separation at the gold−carbon film interface, which can extend the lifetime of hot carriers to promote plasmonic photocatalysts.

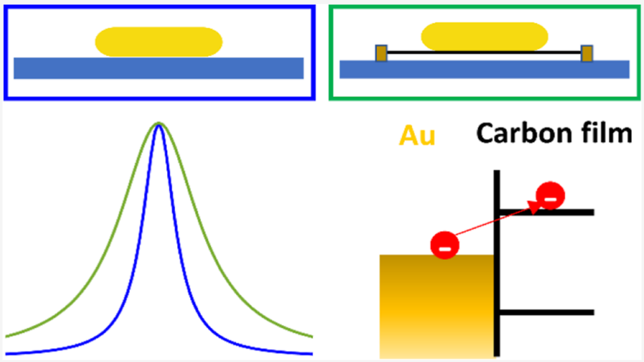

■ INTRODUCTION

Nobel metallic nanoparticles exhibit unique optical and physical properties due to surface plasmon resonances, the collective oscillation of conduction band electrons.[1,2] Plasmonic nanostructures have been demonstrated as photocatalysts or electrophotocatalysts to drive various chemical reactions, including NH_3 decomposition,[3,4] CO_2 reduction,[5−12] hydrogen generation,[13−15] and NH_3 formation.[16−19] The superior properties in photocatalysis and photoelectrocatalysis stem from the efficient absorption of photons by plasmons[20] and the generation of high-energy carriers that enable chemical reactions with high activation barriers.[21−29] Moreover, the tunability of plasmon energy by morphologies and compositions of plasmonic nanostructures facilitates photon harvesting in the UV-NIR region.[30−33] Furthermore, the photon energy absorbed by plasmon can transfer to catalytic materials in close proximity to the plasmonic nanostructures, promoting catalytic reactions.[4,34,35]

The photoexcitation of surface plasmon resonances in nanostructures, such as gold (Au) nanoparticles, promotes electrons from the Fermi level of Au to the unoccupied states within the conduction band, creating hot electrons and warm holes above and near the Fermi level, respectively.[36−39] When photons with energy higher than the interband threshold of Au excite electrons from the d-band to the sp-band, warm electrons near the Fermi level of Au and hot d-band holes are generated. These highly energetic carriers, generated by the photoexcitation of plasmonic nanostructures, have been shown to overcome high activation barriers to catalyze chemical reactions.[3−19] However, the short lifetime of plasmon-induced hot carriers (<100 fs),[36,40−46] resulting from ultrafast electron−hole recombination and electron−electron scattering, hinders their utilization in chemical reactions. Therefore, prolonging the lifetime of hot carriers is critical to achieving efficient plasmonic photocatalysts.

Plasmonic nanoparticles decorated with semiconductors, catalytic metals, and molecular adsorbates create charge separation states at heterojunctions to impede ultrafast electron−hole recombination.[47−56] Such strategies have successfully extended the lifetime of hot carriers and greatly enhanced the activities of plasmonic photocatalysts and photocurrent in plasmonic devices.[57] Several mechanisms

Received: November 25, 2023
Revised: December 6, 2023
Accepted: December 8, 2023
Published: December 19, 2023

https://doi.org/10.1021/acs.jpcc.3c07754

have been identified for the charge transfer at the heterojunction of hybrid nanostructures.[20] For example, Au nanoparticles in contact with semiconductors form the Schottky barrier at the Au/semiconductor interface. When plasmons are excited, the electrons populate the unoccupied states within the conduction band in the metal, and the excited electrons with energy higher than the Schottky barrier transfer to the conduction band of the semiconductor.[47] This process refers to an indirect charge transfer. In contrast, the strong interaction between Au and the semiconductor creates hybrid states through the energetic and spatial overlaps of the electron wave functions of the two materials. Direct charge transfer refers to the process in which the electrons in the metal are directly excited to the conduction band of the semiconductor upon plasmon decay.[48] This charge transfer mechanism also occurs in a hybrid structure composed of plasmonic nanostructures and molecular adsorbates.[51−54] The oscillation of the conduction band electrons loses its coherence by transferring the electrons to the LUMO of the adsorbates, leading to faster decay of plasmon. This decay channel resulting from direct electron transfer in the hybrid structure is known as chemical interface damping.[58] Maximizing the charge separation in the hybrid plasmonic nanostructures to increase the lifetime of hot carriers will advance our knowledge to realize plasmonic photocatalysts.

In addition to efficient charge separation at the heterojunction, high electron mobility is also required in the electron acceptor to extract the electrons and impede electron−hole recombination at the Au/semiconductor interface. Two-dimensional (2D) carbon nanostructures, including graphene and amorphous thin films, have demonstrated excellent electron mobility and have been utilized for several applications, such as flexible electronic devices, supercapacitors, and electrodes for batteries.[59−63] Additionally, doping nitrogen atoms into the carbon film or graphene exhibits excellent catalytic activities for various redox reactions.[64−67] Therefore, combining plasmonic nanostructures with 2D carbon materials is an attractive strategy to extend the lifetime of the hot carriers. A decade ago, Hoggard et al. determined electron transfer between Au nanorods (AuNRs) and graphene with ∼10% efficiency upon plasmon excitation.[68] The efficiency was estimated by measuring the scattering and photoluminescence spectra of single AuNRs and comparing their spectral line widths on glass and graphene. As single-particle spectroscopy determines the homogeneous line width that represents the dephasing time of the plasmons, it is possible to estimate the electron transfer rate and efficiency.[68,69] Despite the magnificent demonstration of charge transfer in the AuNR/graphene system, hybrid nanostructures composed of plasmonic nanoparticles and other 2D carbon materials, such as a carbon thin film, have not been explored.

In this study, we fabricated hybrid systems comprising AuNRs and carbon films with various thicknesses and investigated the electron transfer between AuNRs and the carbon film using single-particle dark-field scattering (DFS) spectroscopy. By comparing the spectra of single AuNRs on a glass substrate with those on the carbon film, we observed a much broader spectral line width of AuNRs on the carbon film, indicating an efficient electron transfer in this hybrid nanostructure. The contribution of plasmon-induced resonance energy transfer to plasmon decay was excluded. The electron-transfer efficiency was more than 50% on carbon films with various thicknesses. These results suggest a simple and robust method for creating a hybrid nanostructure with efficient charge separation for plasmonic photocatalysts.

■ EXPERIMENTAL METHODS

Materials. Cetyltrimethylammonium bromide (CTAB)-capped AuNRs (AuNRs, part #: A12-25-700-CTAB-DIH-1-25) were purchased from Nanopartz. PELCO TEM grids with supporting carbon films with thicknesses of 10 nm (part #: 01900) and 25 nm (part #: 01910-F) were purchased from Ted Pella, Inc. Potassium hydroxide (KOH, pellets/certified ACS, part #: P250-1), reagent alcohol (HPLC grade, 89 to 91%, part #: A995-4), acetone (ACS reagent grade, 99.5%, part #: A929-4), Hellmanex III, glass slides (25 × 75 × 1 mm, part#: 12-544-4), and coverslips (25 × 25 mm, part#: 12542C) were purchased from Fisher Scientific. Deionized (DI) water was used in the experiments.

Preparation of AuNRs on TEM Grids. Glass coverslips and glass slides were cleaned by sonication in Hellmanex (2%), reagent alcohol, acetone, KOH (1 M), and DI water. The TEM grid was attached to a cleaned coverslip with carbon tape. The diluted CTAB-capped AuNR solution was then spin-coated onto the coverslip. The coverslip was assembled into a cell with a glass side using carbon tape as a spacer. A schematic illustration of the cell fabrication process is shown in Figure S1.

Single-Particle Dark-Field Scattering Microscopy. The scattering spectra of AuNRs were measured by a custom-built DFS microscope composed of an inverted microscope body (Zeiss, Axio-Observer 5) and a spectrometer (Princeton Instrument, ARC-SP-2156) equipped with a charge-coupled device camera (Princeton Instrument, PIX-400BRX) mounted on a motorized linear stage (Newport, CONEX-LTA-HL). A halogen lamp (Zeiss, HAL-100) was used as the light source. The white light from the lamp passed through the dark-field condenser (N.A. = 1.4) and focused on the sample. The scattered light from AuNRs was collected by an oil immersion objective (Zeiss, PlanAchromat, N.A. = 0.7, 63×) directed to the spectrometer located at the first image plane of the microscope. A custom-written Labview program was used to control the motorized linear stage and the spectrometer to scan the slit of the spectrometer through the scattering image while taking spectra to enable hyperspectral imaging. The analyses of the hyperspectral images were performed by the Matlab program developed in the lab. The scattering spectra of AuNRs were background-subtracted and normalized by the lamp spectrum.

Scanning Electron Microscopy. The SEM images were performed on a Hitachi SU5000 SEM with an acceleration voltage of 10 kV. For the correlation between SEM and single-particle measurements, the optical and hyperspectral images were acquired before the SEM characterizations to avoid the melting of AuNRs by the strong e-beam radiation.

■ RESULTS AND DISCUSSION

In order to investigate the damping of surface plasmon resonances on a carbon film, we measured the scattering spectra of single AuNRs on the carbon film and glass substrate. A TEM grid (Figure S2) with a supporting carbon film with a thickness of 25 nm was attached to a coverslip by using carbon tape. The thickness of the carbon film was provided by the manufacturer. The solution of AuNRs was spin-coated on the coverslip to allow AuNRs to spread on the TEM grid and the coverslip with a proper density for single-particle measurements. The size of the AuNRs was quantified as 29.6 ± 3.9 × 87.9 ± 12.6 nm with an aspect ratio of 3.0 ± 0.6, as shown in Figure S3. The substrate was assembled into a cell with another microscope slide spaced by carbon tape and mounted on a DFS microscope. Hyperspectral images of AuNRs on glass and carbon film were acquired in the same cell. The intensities of different AuNRs can be directly compared, considering that the hyperspectral images were measured under identical conditions. Figure 1A,B shows schematic illustrations of a single AuNR on glass and carbon film, respectively. As the carbon film hosted by the copper grid was suspended above the glass substrate (Figure 1B), it is possible to identify the interfaces of air/carbon film and air/glass by moving the focus of the objective (Figure S4).

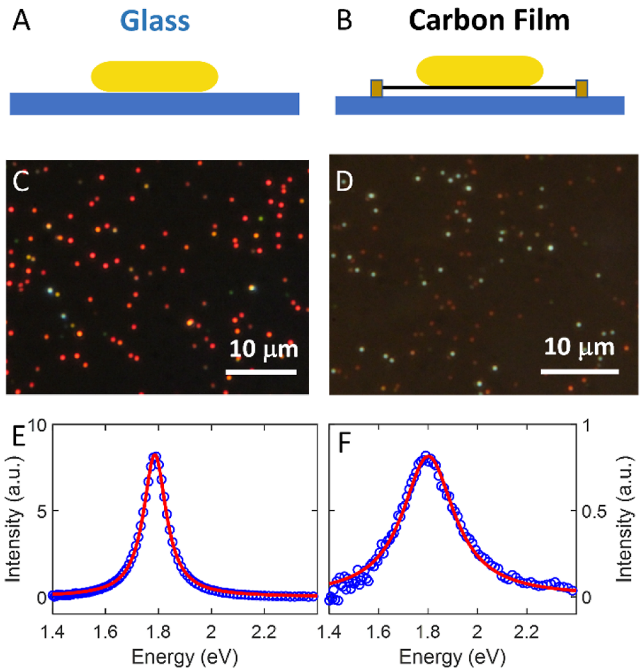

Figure 1. Optical properties of AuNRs on glass and carbon film. (A,B) Schematic illustration of a AuNR on a glass substrate (A) and on a TEM grid supported by a carbon film (B). The blue, black, and dark yellow colors represent glass, carbon film, and copper grid, respectively. (C,D) Color images of AuNR scattering on glass (C) and carbon film (D). (E,F) Representative scattering spectra (symbol) of single AuNR on glass (E) and carbon film (F). The red lines are the fitting curve to the Lorentzian function.

The scattering spectra of AuNRs on the carbon film were strongly damped. Figure 1C shows the scattering image of AuNRs on glass taken by a single-lens refraction camera inserted at the position of the eyepiece of the microscope. The image of AuNRs on the glass was taken at the region outside the TEM grid. The bright and sharp red color originates from the scattering of single AuNRs, which is consistent with the literature.[70] In contrast, the scattering image of AuNRs on the carbon film appears dark red with low intensity, suggesting a significant quenching of AuNR scattering (Figure 1D). Hyperspectral images at positions identical to those in Figure 1C,D were acquired to obtain the scattering spectra of individual AuNRs. The resulting scattering spectra were fit to the Lorentzian function to obtain the peak energy (E_{res}), the full width at half-maximum (Γ), and peak intensity (I_{max}), as displayed in Figure S5. Figure 1E,F shows the scattering spectra (symbol) of a representative AuNR on glass and carbon film, respectively. The scattering spectra fit very well with the Lorentzian function (red line), suggesting that the scattering originates from single AuNRs. When comparing the AuNR spectra in Figure 1E,F, the scattering of AuNRs on the carbon film was strongly quenched. In Figure 1F, the Γ of AuNR on the carbon film is 256, 151 meV higher than that on glass (105 meV) shown in Figure 1E. The peak intensity of AuNR on glass (I_{max} = 8.24) is ∼10-fold higher than that on the carbon film (I_{max} = 0.81). The broader spectral line width with lower intensity in the scattering spectrum indicates significant damping of the surface plasmon resonance of AuNRs on the carbon film.

To confirm that the broad spectrum shown in Figure 1F originates from a single AuNR rather than its aggregate, we performed optical measurements and SEM characterizations in identical regions. The indexed TEM grid allows for locating the same AuNRs with the optical and electron microscopes. Figure 2A,B shows the optical and SEM images of AuNRs in the identical region, respectively. Squares with the same colors indicate the same particles in both images. We observed that the dim red spots in Figure 2A correspond to the single AuNRs shown in Figure 2B, supported by the high-magnification SEM images (Figure 2C). Furthermore, the white spots in Figure 2A are the result of the defects in the carbon film, as shown in the white circles in Figure 2B. A hyperspectral image of the same location was acquired and the scattering spectra of the AuNRs were analyzed. Figure 2D displays the scattering spectra (symbol) of the AuNRs marked by the squares in Figure 2B. The color code of the spectra is identical to that of the squares. Fitting with the Lorentzian function (color lines), Γ is in the range of 223−272 meV, confirming that the spectral line width of the AuNRs on the carbon film is much broader, consistent with the result shown in Figure 1F.

The line width broadening of the AuNR scattering was observed on the carbon films with various thicknesses. AuNRs were deposited on TEM grids with carbon film thicknesses of 10 and 25 nm attached to coverslips, each of which was assembled into a cell. Scattering spectra of 1259, 853, and 330 AuNRs were measured on glass and carbon films with thicknesses of 25 and 10 nm, respectively, to obtain statistical information on plasmon damping. Figure 3A−C shows the cumulative distribution of E_{res} (A), Γ (B), and normalized I_{max} (C) for single AuNRs on glass (blue) and carbon films with thicknesses of 10 (red) and 25 nm (green). The cumulative distribution represents the fraction of AuNRs with a value lower than the one indicated in the x-axis. E_{res} of the AuNRs on carbon films (1.80 ± 0.11 eV for 25 nm and 1.77 ± 0.11 eV for 10 nm) are red-shifted compared to those on glass (1.86 ± 0.12 eV), as shown in Figure 3A, due to the higher refractive index of the amorphous carbon film ($n \sim 2.00$) than glass ($n = 1.50$).[71] By comparing the line width shown in Figure 3B, Γ values of AuNRs on carbon films with thicknesses of 10 and 25 nm are 232.7 ± 28.1 and 255.3 ± 31.5 meV, respectively. These values are two times higher than the Γ of AuNRs on glass (119.6 ± 19.6 meV). The broader line width observed on the carbon film is independent of AuNR orientation (Figure S6). To compare the I_{max} values of AuNRs measured between different cells, we normalized all I_{max} values of every AuNR with the mean values of AuNRs on glass for each cell to account for the intercell variation in illumination intensity from the lamp. Figure 3C shows the cumulative distribution of the

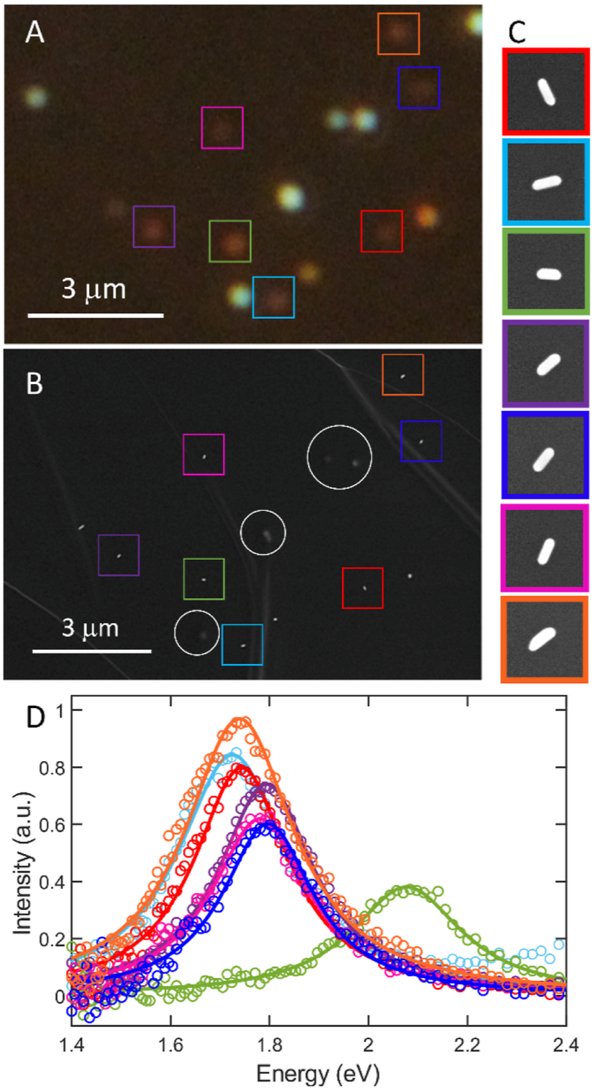

Figure 2. Correlation between optical and SEM images. (A,B) Scattering (A) and SEM (B) images of AuNRs on a carbon film. The color boxes indicate the same AuNRs on optical and SEM images. The scale bar is 3 μm. (C) SEM images of AuNRs at higher magnification. The size of the images is 300 × 300 nm. The color boxes represent the AuNRs marked with the same color boxes in (A and B). (D) Scattering spectra of AuNRs marked by the boxes in (A–C). The color code of the spectra is identical to that of the color boxes.

normalized I_{max} values of AuNRs on different substrates. The normalized I_{max} values of AuNRs on carbon films are only ~20% of those on glass. Combining the evidence of a broader line width and weak intensity of AuNR scattering, we can conclude that surface plasmon resonance is significantly damped when AuNRs are in contact with a carbon film.

Previous studies have demonstrated that the longitudinal plasmon damping of AuNRs in the hybrid system could arise from plasmon-induced resonance energy transfer or charge transfer.[20] It is known that plasmons decay on the order of 5–20 fs, which is challenging to probe using time-resolved spectroscopy.[72−75] Alternatively, one can measure the homogeneous line width of single nanoparticles because the spectral width is proportional to the plasmon decay rate.[69] In the plasmonic hybrid system, it is accepted that the homogeneous line width is mainly contributed by four decay channels, including bulk damping γ_b, electron surface damping Γ_{suf}, radiation damping Γ_{rad}, and damping due to plasmon-induced resonance energy transfer or charge transfer $\Gamma_{RET/CT}$.[51,76]

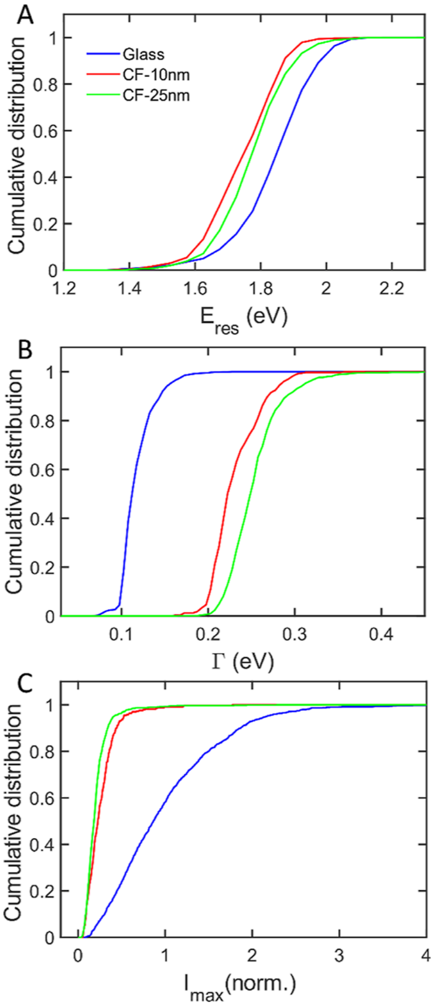

Figure 3. Statistics of the spectral parameters of AuNR scattering on different substrates. (A–C) Cumulative distributions of E_{res} (A), Γ (B), and normalized I_{max} of scattering spectra for AuNRs on glass (blue) and carbon films (CF) with thicknesses of 10 (red) and 25 nm (green). The statistical information includes the spectra of 1259, 853, and 330 AuNRs on glass and carbon films with thicknesses of 25 and 10 nm, respectively.

$$\Gamma = \gamma_b + \Gamma_{surf} + \Gamma_{rad} + \Gamma_{RET/CT}$$

Bulk damping arises from the electron scattering with thermal phonons and impurities inside the metal and behaves the same as bulk materials, including the contribution from the interband transition. Electron surface damping describes the electron scattering at the nanoparticle surface and is dominant when the nanoparticle size is smaller than the mean free path of the metal. Radiation damping results from the damping of plasmons into far-field radiation and increases with a larger volume of nanoparticles. These three terms are intrinsic to nanoparticles with a known size. In the hybrid system composed of plasmonic nanoparticles with the semiconductor or molecular adsorbates, additional dampings such as plasmon-induced energy transfer or charge transfer further increase the spectral line width.

The additional damping, $\Gamma_{RET/CT}$, of AuNRs on the carbon film can be quantified by the changes in line width from the DFS spectra. Figure 4A displays Γ vs E_{res} of AuNRs on glass (blue) and carbon films with thicknesses of 10 (red) and 25 nm (green). The gray shadow represents the contribution of bulk damping, calculated based on the procedure in the previous report.[77] The bulk damping increases when the plasmon energy is higher than the interband threshold (1.76 eV) and is constant with plasmon energy lower than 1.76 eV. This contribution is clearly observed for the AuNRs on glass, where Γ becomes larger when E_{res} is greater than 1.76 eV (blue symbol). The measured line width on the glass substrate is slightly higher than the bulk damping, resulting from the contribution of radiation damping, given the AuNR dimension of 29.6 ± 3.9 × 87.9 ± 12.6 nm. At this size, electron surface damping is negligible because the diameter and length of AuNRs are higher than the mean free path of Au. When comparing the line widths of the scattering spectra for AuNRs on different substrates, the experimental Γ on the carbon film (green and red symbols) increase more than 100 meV than those on glass regardless of the value of E_{res}, while Γ is slightly larger on the thicker carbon film (green vs red symbols). The line width of AuNR scattering on glass represents the intrinsic line width ($\Gamma_0 = \gamma_b + \Gamma_{surf} + \Gamma_{rad}$) because the glass substrate does not introduce additional plasmon damping due to the large band gap. The damping arising from plasmon-induced resonance energy transfer or charge transfer does not occur at the AuNR/glass interface. Several studies have represented intrinsic line width using the scattering line width of AuNRs on a glass substrate.[49,51,54,68,76,78] Measuring the line width of the same AuNR on a carbon film ($\Gamma = \Gamma_0 + \Gamma_{RET/CT}$) enables quantifying $\Gamma_{RET/CT}$ for additional damping due to the coupling between plasmon and the carbon film. To accurately determine $\Gamma_{RET/CT,}$ it is necessary to measure the line width difference of the scattering spectra from the same AuNRs on glass and the carbon film. However, it is infeasible in our measurements because we cannot relocate AuNRs from the glass to the carbon film on the TEM grid. Instead, we measured the average Γ of AuNRs on the glass to represent the intrinsic line width (Γ_0), which is subtracted from Γ for every AuNR on the carbon film to obtain the apparent $\Gamma_{RET/CT}$. In this analysis, only AuNRs with an E_{res} of less than 1.76 eV were calculated to eliminate the contribution of the energy-dependent interband transition. In this case, the variation of Γ for AuNRs on glass mainly arises from the radiation damping with heterogeneous size distribution because the surface scattering plays a minor role at this size. Figure 4B illustrates the cumulative distribution of the apparent $\Gamma_{RET/CT}$ with 10 (red) and 25 nm (green) carbon films. The apparent $\Gamma_{RET/CT}$ values are 142 ± 25 and 116 ± 26 meV for 25 and 10 nm carbon films, respectively. Previous studies have investigated charge transfer in the hybrid nanostructures composed of AuNRs and monolayer graphene and demonstrated Γ_{CT} of ~10 meV,[68] which is 1 order of magnitude smaller than the apparent $\Gamma_{RET/CT}$ on carbon film. The longitudinal plasmon of AuNR is only slightly damped on graphene and is severely damped on the carbon film. Combining the results of charge transfer on graphene and $\Gamma_{RET/CT}$ on the carbon film shown in Figure 4B, we can conclude that the damping of the longitudinal plasmons increases with thicker 2D carbon nanostructures.

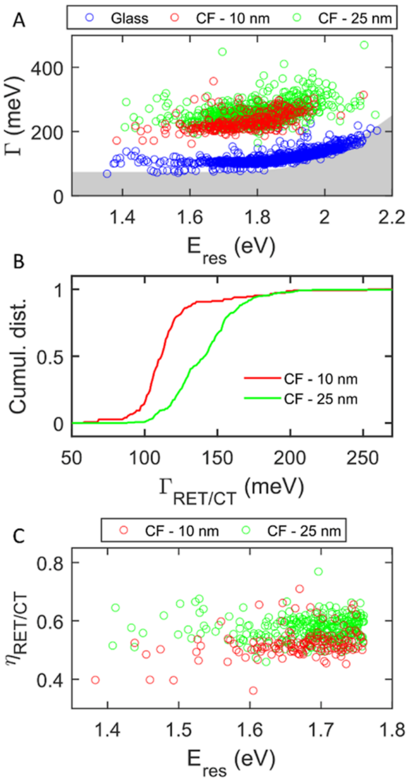

Figure 4. Plasmon damping efficiencies on the carbon films with different thicknesses. (A) Γ as a function of E_{res} for AuNRs on glass (blue) and carbon films (CF) with thicknesses of 10 (red) and 25 nm (green). The gray area represents the bulk damping, including the contribution from interband transition. (B) Cumulative distribution of the apparent $\Gamma_{RET/CT}$ for AuNRs on carbon films with thicknesses of 10 (red) and 25 nm (green). (C) $\eta_{RET/CT}$ as a function of E_{res} for AuNRs on carbon films with thicknesses of 10 (red) and 25 nm (green).

The efficiency of plasmon damping, $\eta_{RET/CT}$, due to resonance energy transfer or charge transfer is further quantified from $\eta_{RET/CT} = {}^{\Gamma_{RET/CT}}/_{\Gamma}$, where Γ is the line width of AuNR on the carbon film. Figure 4C illustrates the $\eta_{RET/CT}$ of single AuNRs as a function of their E_{res} on the carbon films with 10 (red) and 25 nm (green) thicknesses. Only AuNRs with an E_{res} smaller than 1.76 eV were calculated to avoid the contribution of the energy-dependent interband transition. The efficiencies of plasmon damping, $\eta_{RET/CT}$, of AuNRs on the carbon films with 10 and 25 nm are 52.8 ± 4.8 and 57.4 ± 4.0%, respectively. These two values are more than five times higher than the charge transfer efficiency in the AuNR/graphene hybrid nanostructure.

The plasmon damping on the carbon film arises from plasmon-induced charge transfer rather than plasmon-induced resonance energy transfer. In a hybrid system composed of Au and semiconductor nanostructures, plasmon-induced charge transfer occurs at the Au/semiconductor interface through direct or indirect charge transfer pathways after plasmon excitation.[20] The efficiency of this interfacial charge transfer highly depends on the electronic structures and electron wave function overlap between Au and the semiconductor.[27,47,48] The plasmon-induced resonance energy transfer originates from the strong dipole−dipole interaction between plasmonic and semiconductor materials.[79] Upon excitation of the plasmon, the plasmon energy in the metal nonradiatively transfers to the semiconductor, creating electrons and holes in the conduction and valence bands, respectively. The efficiency of energy transfer is regulated by the interfacial electric conductivity, the dipole strength of donors and acceptors, and the spectral overlap of the plasmon and absorption spectrum of the semiconductor.[79−81] Plasmon-induced resonance energy transfer has been applied to enhance the efficiency of solar cells because it allows harvesting of the plasmon energy before ultrafast decay of the plasmon within 20 fs.[79−81] Both charge transfer and resonance energy transfer in the hybrid system cause strong damping in the surface plasmon resonances due to the additional relaxation pathways for plasmon.[49,76] To confirm the mechanism of plasmon damping on the carbon film, we compare $\eta_{\mathrm{RET/CT}}$ as a function of E_{res} with the absorption spectra of the carbon film. As shown in Figure 4C, $\eta_{\mathrm{RET/CT}}$ of AuNRs only exhibits a small variation without a clear trend, with the E_{res} value at 1.35−1.76 eV. The variation of $\eta_{\mathrm{RET/CT}}$ at the same E_{res} possibly results from the size dispersion of AuNRs. To clearly identify if $\eta_{\mathrm{RET/CT}}$ depends on the E_{res} of scattering spectra, we further average $\eta_{\mathrm{RET/CT}}$ for single AuNRs with E_{res} in bins of 0.5 eV. Figure S7A shows the average $\eta_{\mathrm{RET/CT}}$ as a function of binned E_{res} for AuNRs on carbon films of 10 (red) and 25 nm (green). The symbols and error bars represent the mean and standard deviation of the values with bins of 0.5 eV in E_{res}. AuNRs with $E_{\mathrm{res}} < 1.5$ eV were binned at one data point because a small number of AuNRs peaked at this energy. The average $\eta_{\mathrm{RET/CT}}$ is constant with plasmon energy at 1.35−1.76 eV on the carbon film, except for one data point, which shows a lower $\eta_{\mathrm{RET/CT}}$ with $E_{\mathrm{res}} < 1.5$ eV on the thinner film. Figure S7B displays the absorption spectra of the carbon films with thicknesses of 10 (red) and 25 nm (green) measured at an area of 1 × 1 μm. Each absorption spectrum was averaged from the spectra collected at ten different locations to account for the local thickness variation. The absorption of the carbon film increases with energy for both thicknesses, consistent with the absorption spectrum of the amorphous carbon film reported previously.[82] For the plasmon-induced resonance energy transfer, the efficiency is proportional to the spectral overlap between the plasmon band and the absorption spectra of the carbon film. In this case, the average $\eta_{\mathrm{RET/CT}}$ as a function of binned E_{res} is expected to increase with the plasmon energy. By comparing the results in Figure S7, we exclude the contribution of resonance energy transfer and conclude that charge transfer is responsible for the line width broadening on the carbon film. The energy-independent $\eta_{\mathrm{RET/CT}}$ observed in our study is also consistent with the report of the Au/CdSe hybrid system, where the quantum yield of the Au-to-CdSe charge transfer is constant with the excitation energy below the interband gap of CdSe NRs.[48] The origin of a slightly smaller $\eta_{\mathrm{RET/CT}}$ on a thinner carbon film is unclear and requires further investigation.

This study demonstrated a robust and simple method for fabricating hybrid nanostructures by spin- or drop-casting a colloidal solution of Au nanoparticles on the carbon film. The efficient charge transfer at the Au/carbon film interface prohibits ultrafast electron−hole recombination after plasmon excitation and produces long-lived hot carriers that enhance plasmonic photocatalysis. The efficiency of charge transfer at the interface of Au and carbon film is 57.4 ± 4.0% comparable to η_{CT} of 50 ± 18% for Ag-$\mathrm{CsPbBr_3}$ hybrid nanocrystals, which exhibit the most efficient plasmon-induced charge transfer to date.[83] Additionally, CTAB capping ligands adsorb on the AuNR surface. Therefore, the charge transfer efficiency can further increase in the AuNR/carbon film system by removing CTAB from the AuNR surface to increase the contact area between the AuNR and the carbon film. All of these results suggest that the hybrid nanostructure composed of Au nanoparticles and carbon film can be a robust and efficient plasmonic photocatalyst.

■ CONCLUSIONS

In summary, we utilized single-particle DFS spectroscopy to measure the homogeneous line width of a longitudinal plasmon of single AuNRs on a glass substrate and carbon films and observed a line width broadening of >100 meV on carbon films. Correlating between the optical and SEM images in the identical region confirmed the broad spectra originating from single AuNRs on the carbon film, indicating additional and strong plasmon damping. The damping efficiencies were determined as 52.8 ± 4.8 and 57.4 ± 4.0% for 10 and 25 nm films, respectively. We attributed this plasmon damping to electron transfer from AuNRs to the carbon film rather than plasmon-induced resonant energy transfer after careful analysis of the energy-dependent efficiency and absorption spectra of the carbon films. The charge transfer efficiency of 57.4 ± 4.0% in the AuNR/carbon film structure is comparable to that of 50 ± 18% for Ag/$\mathrm{CsPbBr_3}$ hybrid nanocrystals, which is known as the most efficient plasmon-induced charge transfer to date. We anticipate that this value will be further improved by removing the CTAB ligands to increase the contact between AuNRs and the carbon film. The efficient charge transfer in the AuNR/carbon film hybrid structure and the high conductivity of the carbon film can extend the hot carrier lifetime and facilitate the harvest of hot carriers, both of which are critical to realizing the plasmonic photocatalysts.

■ ASSOCIATED CONTENT

Supporting Information

The Supporting Information is available free of charge at https://pubs.acs.org/doi/10.1021/acs.jpcc.3c07754.

Procedures of dry cell assembly; SEM images of the TEM grid and AuNRs; color images of AuNRs at different focuses; scattering spectrum of a AuNR fit to the Lorentzian function; Line width of AuNRs on a carbon film as a function of AuNR orientation; and binned $\eta_{\mathrm{RET/CT}}$ and absorption spectra of carbon films (PDF)

■ AUTHOR INFORMATION

Corresponding Author

Wei-Shun Chang − *Department of Chemistry and Biochemistry, University of Massachusetts Dartmouth, North Dartmouth, Massachusetts 02747, United States;* orcid.org/0000-0002-0251-4449; Email: wchang2@umassd.edu

Author

Tamie Vo − *Department of Chemistry and Biochemistry, University of Massachusetts Dartmouth, North Dartmouth, Massachusetts 02747, United States;* orcid.org/0009-0003-7681-0966

Complete contact information is available at: https://pubs.acs.org/10.1021/acs.jpcc.3c07754

Author Contributions

T.V. and W.-S.C. conceived the idea and designed the experiments. T.V. formed experiments and analyzed the data. W.-S.C. wrote the manuscript with contributions from T.V. All authors have given their approval of the manuscript.

Notes

The authors declare no competing financial interest.

■ ACKNOWLEDGMENTS

This work is supported by the ACS Petroleum Research Fund (62122-DNI6) and the National Science Foundation (CHE 2203612, CMI program) with partial cofunding from the CAT, MSN, and CSDM-A programs. The electron microscopy images in this work were obtained using a scanning electron microscope supported by the National Science Foundation under Grant no. 1726239.

■ REFERENCES

(1) Maier, S. A. *Plasmonics: Fundamentals and Applications*; Springer: New York, 2007.

(2) Lal, S.; Link, S.; Halas, N. J. Nano-Optics from Sensing to Waveguiding. *Nat. Photonics* **2007**, *1*, 641−648.

(3) Yuan, Y.; Zhou, L.; Robatjazi, H.; Bao, J. L.; Zhou, J.; Bayles, A.; Yuan, L.; Lou, M.; Lou, M.; Khatiwada, S.; et al. Earth-Abundant Photocatalyst for H_2 Generation from NH_3 with Light-Emitting Diode Illumination. *Science* **2022**, *378*, 889−893.

(4) Zhou, L.; Swearer, D. F.; Zhang, C.; Robatjazi, H.; Zhao, H.; Henderson, L.; Dong, L.; Christopher, P.; Carter, E. A.; Nordlander, P.; et al. Quantifying Hot Carrier and Thermal Contributions in Plasmonic Photocatalysis. *Science* **2018**, *362*, 69−72.

(5) DuChene, J. S.; Tagliabue, G.; Welch, A. J.; Cheng, W.-H.; Atwater, H. A. Hot Hole Collection and Photoelectrochemical Co2 Reduction with Plasmonic Au/P-Gan Photocathodes. *Nano Lett.* **2018**, *18*, 2545−2550.

(6) Yu, S.; Wilson, A. J.; Heo, J.; Jain, P. K. Plasmonic Control of Multi-Electron Transfer and C-C Coupling in Visible-Light-Driven Co2 Reduction on Au Nanoparticles. *Nano Lett.* **2018**, *18*, 2189−2194.

(7) Creel, E. B.; Corson, E. R.; Eichhorn, J.; Kostecki, R.; Urban, J. J.; McCloskey, B. D. Directing Selectivity of Electrochemical Carbon Dioxide Reduction Using Plasmonics. *ACS Energy Lett.* **2019**, *4*, 1098−1105.

(8) Robatjazi, H.; Zhao, H.; Swearer, D. F.; Hogan, N. J.; Zhou, L.; Alabastri, A.; McClain, M. J.; Nordlander, P.; Halas, N. J. Plasmon-Induced Selective Carbon Dioxide Conversion on Earth-Abundant Aluminum-Cuprous Oxide Antenna-Reactor Nanoparticles. *Nat. Commun.* **2017**, *8*, 27.

(9) Devasia, D.; Wilson, A. J.; Heo, J.; Mohan, V.; Jain, P. K. A Rich Catalog of C-C Bonded Species Formed in Co2 Reduction on a Plasmonic Photocatalyst. *Nat. Commun.* **2021**, *12*, 2612.

(10) Hu, C.; Chen, X.; Low, J.; Yang, Y.-W.; Li, H.; Wu, D.; Chen, S.; Jin, J.; Li, H.; Ju, H.; et al. Near-Infrared-Featured Broadband Co2 Reduction with Water to Hydrocarbons by Surface Plasmon. *Nat. Commun.* **2023**, *14*, 221.

(11) Li, R.; Cheng, W.-H.; Richter, M. H.; DuChene, J. S.; Tian, W.; Li, C.; Atwater, H. A. Unassisted Highly Selective Gas-Phase Co2 Reduction with a Plasmonic Au/P-Gan Photocatalyst Using H2o as an Electron Donor. *ACS Energy Lett.* **2021**, *6*, 1849−1856.

(12) Lai, H.; Xiao, W.; Wang, Y.; Song, T.; Long, B.; Yin, S.; Ali, A.; Deng, G.-J. Plasmon-Induced Carrier Separation Boosts High-Selective Photocatalytic Co2 Reduction on Dagger-Axe-Like Cu@ Co Core-Shell Bimetal. *Chem. Eng. J.* **2021**, *417*, 129295.

(13) Wang, Y.; Wang, Y.; Aravind, I.; Cai, Z.; Shen, L.; Zhang, B.; Wang, B.; Chen, J.; Zhao, B.; Shi, H.; et al. In Situ Investigation of Ultrafast Dynamics of Hot Electron-Driven Photocatalysis in Plasmon-Resonant Grating Structures. *J. Am. Chem. Soc.* **2022**, *144*, 3517−3526.

(14) Mubeen, S.; Lee, J.; Singh, N.; Krämer, S.; Stucky, G. D.; Moskovits, M. An Autonomous Photosynthetic Device in Which All Charge Carriers Derive from Surface Plasmons. *Nat. Nanotechnol.* **2013**, *8*, 247−251.

(15) Joshi, G.; Saha, A.; Dutta, A.; Khatua, S. Nir-Driven Photocatalytic Hydrogen Production by Silane- and Tertiary Amine-Bound Plasmonic Gold Nanoprisms. *ACS Appl. Mater. Interfaces* **2022**, *14*, 38815−38823.

(16) Oshikiri, T.; Ueno, K.; Misawa, H. Plasmon-Induced Ammonia Synthesis through Nitrogen Photofixation with Visible Light Irradiation. *Angew. Chem., Int. Ed.* **2014**, *53*, 9802−9805.

(17) Hu, C.; Chen, X.; Jin, J.; Han, Y.; Chen, S.; Ju, H.; Cai, J.; Qiu, Y.; Gao, C.; Wang, C.; et al. Surface Plasmon Enabling Nitrogen Fixation in Pure Water through a Dissociative Mechanism under Mild Conditions. *J. Am. Chem. Soc.* **2019**, *141*, 7807−7814.

(18) Oshikiri, T.; Ueno, K.; Misawa, H. Selective Dinitrogen Conversion to Ammonia Using Water and Visible Light through Plasmon-Induced Charge Separation. *Angew. Chem., Int. Ed.* **2016**, *55*, 3942−3946.

(19) Contreras, E.; Nixon, R.; Litts, C.; Zhang, W.; Alcorn, F. M.; Jain, P. K. Plasmon-Assisted Ammonia Electrosynthesis. *J. Am. Chem. Soc.* **2022**, *144*, 10743−10751.

(20) Li, S.; Huang, H.; Shao, L.; Wang, J. How to Utilize Excited Plasmon Energy Efficiently. *ACS Nano* **2021**, *15*, 10759−10768.

(21) Wu, S.; Chen, Y.; Gao, S. Plasmonic Photocatalysis with Nonthermalized Hot Carriers. *Phys. Rev. Lett.* **2022**, *129*, 086801.

(22) Salmón-Gamboa, J. U.; Romero-Gómez, M.; Roth, D. J.; Krasavin, A. V.; Wang, P.; Dickson, W.; Zayats, A. V. Rational Design of Bimetallic Photocatalysts Based on Plasmonically-Derived Hot Carriers. *Nanoscale Adv.* **2021**, *3*, 767−780.

(23) Zhang, Y.; He, S.; Guo, W.; Hu, Y.; Huang, J.; Mulcahy, J. R.; Wei, W. D. Surface-Plasmon-Driven Hot Electron Photochemistry. *Chem. Rev.* **2018**, *118*, 2927−2954.

(24) Brongersma, M. L.; Halas, N. J.; Nordlander, P. Plasmon-Induced Hot Carrier Science and Technology. *Nat. Nanotechnol.* **2015**, *10*, 25−34.

(25) Wang, P.; Krasavin, A. V.; Nasir, M. E.; Dickson, W.; Zayats, A. V. Reactive Tunnel Junctions in Electrically Driven Plasmonic Nanorod Metamaterials. *Nat. Nanotechnol.* **2018**, *13*, 159−164.

(26) Zhang, X.; Chen, Y. L.; Liu, R.-S.; Tsai, D. P. Plasmonic Photocatalysis. *Rep. Prog. Phys.* **2013**, *76*, 046401.

(27) Linic, S.; Aslam, U.; Boerigter, C.; Morabito, M. Photochemical Transformations on Plasmonic Metal Nanoparticles. *Nat. Mater.* **2015**, *14*, 567−576.

(28) Zhang, Z.; Zhang, C.; Zheng, H.; Xu, H. Plasmon-Driven Catalysis on Molecules and Nanomaterials. *Acc. Chem. Res.* **2019**, *52*, 2506−2515.

(29) Zhang, Y.; Nelson, T.; Tretiak, S.; Guo, H.; Schatz, G. C. Plasmonic Hot-Carrier-Mediated Tunable Photochemical Reactions. *ACS Nano* **2018**, *12*, 8415−8422.

(30) Coronado, E. A.; Encina, E. R.; Stefani, F. D. Optical Properties of Metallic Nanoparticles: Manipulating Light, Heat and Forces at the Nanoscale. *Nanoscale* **2011**, *3*, 4042−4059.

(31) Knight, M. W.; Liu, L.; Wang, Y.; Brown, L.; Mukherjee, S.; King, N. S.; Everitt, H. O.; Nordlander, P.; Halas, N. J. Aluminum Plasmonic Nanoantennas. *Nano Lett.* **2012**, *12*, 6000−6004.

(32) Slaughter, L. S.; Chang, W.-S.; Swanglap, P.; Tcherniak, A.; Khanal, B. P.; Zubarev, E. R.; Link, S. Single-Particle Spectroscopy of Gold Nanorods Beyond the Quasi-Static Limit: Varying the Width at Constant Aspect Ratio. *J. Phys. Chem. C* **2010**, *114*, 4934−4938.

(33) Jana, N. R.; Gearheart, L.; Murphy, C. J. Wet Chemical Synthesis of High Aspect Ratio Cylindrical Gold Nanorods. *J. Phys. Chem. B* **2001**, *105*, 4065−4067.

(34) Swearer, D. F.; Zhao, H.; Zhou, L.; Zhang, C.; Robatjazi, H.; Martirez, J. M. P.; Krauter, C. M.; Yazdi, S.; McClain, M. J.; Ringe, E.; et al. Heterometallic Antenna-Reactor Complexes for Photocatalysis. *Proc. Natl. Acad. Sci. U.S.A.* **2016**, *113*, 8916−8920.

(35) Aslam, U.; Chavez, S.; Linic, S. Controlling Energy Flow in Multimetallic Nanostructures for Plasmonic Catalysis. *Nat. Nanotechnol.* **2017**, *12*, 1000−1005.

(36) Bernardi, M.; Mustafa, J.; Neaton, J. B.; Louie, S. G. Theory and Computation of Hot Carriers Generated by Surface Plasmon Polaritons in Noble Metals. *Nat. Commun.* **2015**, *6*, 7044.

(37) Manjavacas, A.; Liu, J. G.; Kulkarni, V.; Nordlander, P. Plasmon-Induced Hot Carriers in Metallic Nanoparticles. *ACS Nano* **2014**, *8*, 7630−7638.

(38) Sundararaman, R.; Narang, P.; Jermyn, A. S.; Goddard Iii, W. A.; Atwater, H. A. Theoretical Predictions for Hot-Carrier Generation from Surface Plasmon Decay. *Nat. Commun.* **2014**, *5*, 5788.

(39) Govorov, A. O.; Zhang, H.; Gun'ko, Y. K. Theory of Photoinjection of Hot Plasmonic Carriers from Metal Nanostructures into Semiconductors and Surface Molecules. *J. Phys. Chem. C* **2013**, *117*, 16616−16631.

(40) Brown, A. M.; Sundararaman, R.; Narang, P.; Goddard, W. A., III; Atwater, H. A. Nonradiative Plasmon Decay and Hot Carrier Dynamics: Effects of Phonons, Surfaces, and Geometry. *ACS Nano* **2016**, *10*, 957−966.

(41) Hartland, G. V.; Besteiro, L. V.; Johns, P.; Govorov, A. O. What's So Hot About Electrons in Metal Nanoparticles? *ACS Energy Lett.* **2017**, *2*, 1641−1653.

(42) Lee, S. A.; Kuhs, C. T.; Searles, E. K.; Everitt, H. O.; Landes, C. F.; Link, S. D-Band Hole Dynamics in Gold Nanoparticles Measured with Time-Resolved Emission Upconversion Microscopy. *Nano Lett.* **2023**, *23*, 3501−3506.

(43) Jeffries, W. R.; Park, K.; Vaia, R. A.; Knappenberger, K. L., Jr Resolving Electron−Electron Scattering in Plasmonic Nanorod Ensembles Using Two-Dimensional Electronic Spectroscopy. *Nano Lett.* **2020**, *20*, 7722−7727.

(44) Voisin, C.; Del Fatti, N.; Christofilos, D.; Vallée, F. Ultrafast Electron Dynamics and Optical Nonlinearities in Metal Nanoparticles. *J. Phys. Chem. B* **2001**, *105*, 2264−2280.

(45) Harutyunyan, H.; Martinson, A. B. F.; Rosenmann, D.; Khorashad, L. K.; Besteiro, L. V.; Govorov, A. O.; Wiederrecht, G. P. Anomalous Ultrafast Dynamics of Hot Plasmonic Electrons in Nanostructures with Hot Spots. *Nat. Nanotechnol.* **2015**, *10*, 770−774.

(46) Hogan, N.; Wu, S.; Sheldon, M. Photothermalization and Hot Electron Dynamics in the Steady State. *J. Phys. Chem. C* **2020**, *124*, 4931−4945.

(47) Knight, M. W.; Sobhani, H.; Nordlander, P.; Halas, N. J. Photodetection with Active Optical Antennas. *Science* **2011**, *332*, 702−704.

(48) Wu, K.; Chen, J.; McBride, J. R.; Lian, T. Efficient Hot-Electron Transfer by a Plasmon-Induced Interfacial Charge-Transfer Transition. *Science* **2015**, *349*, 632−635.

(49) Foerster, B.; Hartelt, M.; Collins, S. S. E.; Aeschlimann, M.; Link, S.; Sönnichsen, C. Interfacial States Cause Equal Decay of Plasmons and Hot Electrons at Gold-Metal Oxide Interfaces. *Nano Lett.* **2020**, *20*, 3338−3343.

(50) Tagliabue, G.; DuChene, J. S.; Abdellah, M.; Habib, A.; Gosztola, D. J.; Hattori, Y.; Cheng, W.-H.; Zheng, K.; Canton, S. E.; Sundararaman, R.; et al. Ultrafast Hot-Hole Injection Modifies Hot-Electron Dynamics in Au/P-Gan Heterostructures. *Nat. Mater.* **2020**, *19*, 1312−1318.

(51) Foerster, B.; Joplin, A.; Kaefer, K.; Celiksoy, S.; Link, S.; Sönnichsen, C. Chemical Interface Damping Depends on Electrons Reaching the Surface. *ACS Nano* **2017**, *11*, 2886−2893.

(52) Foerster, B.; Spata, V. A.; Carter, E. A.; Sönnichsen, C.; Link, S. Plasmon Damping Depends on the Chemical Nature of the Nanoparticle Interface. *Sci. Adv.* **2019**, *5*, No. eaav0704.

(53) Zijlstra, P.; Paulo, P. M. R.; Yu, K.; Xu, Q.-H.; Orrit, M. Chemical Interface Damping in Single Gold Nanorods and Its near Elimination by Tip-Specific Functionalization. *Angew. Chem., Int. Ed.* **2012**, *51*, 8352−8355.

(54) Lee, S. Y.; Tsalu, P. V.; Kim, G. W.; Seo, M. J.; Hong, J. W.; Ha, J. W. Tuning Chemical Interface Damping: Interfacial Electronic Effects of Adsorbate Molecules and Sharp Tips of Single Gold Bipyramids. *Nano Lett.* **2019**, *19*, 2568−2574.

(55) Xiang, B.; Li, Y.; Pham, C. H.; Paesani, F.; Xiong, W. Ultrafast Direct Electron Transfer at Organic Semiconductor and Metal Interfaces. *Sci. Adv.* **2017**, *3*, No. e1701508.

(56) Roche, B.; Vo, T.; Chang, W.-S. Promoting Plasmonic Photocatalysis with Ligand-Induced Charge Separation under Interband Excitation. *Chem. Sci.* **2023**, *14*, 8598−8606.

(57) Cortés, E.; Besteiro, L. V.; Alabastri, A.; Baldi, A.; Tagliabue, G.; Demetriadou, A.; Narang, P. Challenges in Plasmonic Catalysis. *ACS Nano* **2020**, *14*, 16202−16219.

(58) Persson, B. N. J. Polarizability of Small Spherical Metal Particles: Influence of the Matrix Environment. *Surf. Sci.* **1993**, *281*, 153−162.

(59) Kyeremateng, N. A.; Brousse, T.; Pech, D. Microsupercapacitors as Miniaturized Energy-Storage Components for on-Chip Electronics. *Nat. Nanotechnol.* **2017**, *12*, 7−15.

(60) Kim, S. J.; Choi, K.; Lee, B.; Kim, Y.; Hong, B. H. Materials for Flexible, Stretchable Electronics: Graphene and 2d Materials. *Annu. Rev. Mater. Res.* **2015**, *45*, 63−84.

(61) Cai, X.; Lai, L.; Shen, Z.; Lin, J. Graphene and Graphene-Based Composites as Li-Ion Battery Electrode Materials and Their Application in Full Cells. *J. Mater. Chem. A* **2017**, *5*, 15423−15446.

(62) Kim, I.-S.; Shim, C.-E.; Kim, S. W.; Lee, C.-S.; Kwon, J.; Byun, K.-E.; Jeong, U. Amorphous Carbon Films for Electronic Applications. *Adv. Mater.* **2023**, *35*, 2204912.

(63) Park, S.; Vosguerichian, M.; Bao, Z. A Review of Fabrication and Applications of Carbon Nanotube Film-Based Flexible Electronics. *Nanoscale* **2013**, *5*, 1727−1752.

(64) Wang, H.; Maiyalagan, T.; Wang, X. Review on Recent Progress in Nitrogen-Doped Graphene: Synthesis, Characterization, and Its Potential Applications. *ACS Catal.* **2012**, *2*, 781−794.

(65) Geng, D.; Chen, Y.; Chen, Y.; Li, Y.; Li, R.; Sun, X.; Ye, S.; Knights, S. High Oxygen-Reduction Activity and Durability of Nitrogen-Doped Graphene. *Energy Environ. Sci.* **2011**, *4*, 760−764.

(66) Behan, J. A.; Mates-Torres, E.; Stamatin, S. N.; Domínguez, C.; Iannaci, A.; Fleischer, K.; Hoque, M. K.; Perova, T. S.; García-Melchor, M.; Colavita, P. E. Untangling Cooperative Effects of Pyridinic and Graphitic Nitrogen Sites at Metal-Free N-Doped Carbon Electrocatalysts for the Oxygen Reduction Reaction. *Small* **2019**, *15*, 1902081.

(67) Guo, D.; Shibuya, R.; Akiba, C.; Saji, S.; Kondo, T.; Nakamura, J. Active Sites of Nitrogen-Doped Carbon Materials for Oxygen Reduction Reaction Clarified Using Model Catalysts. *Science* **2016**, *351*, 361−365.

(68) Hoggard, A.; Wang, L.-Y.; Ma, L.; Fang, Y.; You, G.; Olson, J.; Liu, Z.; Chang, W.-S.; Ajayan, P. M.; Link, S. Using the Plasmon Linewidth to Calculate the Time and Efficiency of Electron Transfer between Gold Nanorods and Graphene. *ACS Nano* **2013**, *7*, 11209−11217.

(69) Sönnichsen, C.; Franzl, T.; Wilk, T.; von Plessen, G.; Feldmann, J.; Wilson, O.; Mulvaney, P. Drastic Reduction of Plasmon Damping in Gold Nanorods. *Phys. Rev. Lett.* **2002**, *88*, 077402.

(70) Celiksoy, S.; Ye, W.; Wandner, K.; Schlapp, F.; Kaefer, K.; Ahijado-Guzmán, R.; Sönnichsen, C. Plasmonic Nanosensors for the Label-Free Imaging of Dynamic Protein Patterns. *J. Phys. Chem. Lett.* **2020**, *11*, 4554−4558.

(71) Dabaghyan, G. A.; Matevosyan, L. M.; Avjyan, K. E. Determination of Refractive Index and Thickness of Nanosized Amorphous Carbon Films Via Visible Range Reflectance Spectra. *J. Contemp. Phys.* **2019**, *54*, 185−187.

(72) Lamprecht, B.; Krenn, J. R.; Leitner, A.; Aussenegg, F. R. Particle-Plasmon Decay-Time Determination by Measuring the Optical near-Field's Autocorrelation: Influence of Inhomogeneous Line Broadening. *Appl. Phys. B: Lasers Opt.* **1999**, *69*, 223−227.

(73) Liau, Y.-H.; Unterreiner, A. N.; Chang, Q.; Scherer, N. F. Ultrafast Dephasing of Single Nanoparticles Studied by Two-Pulse Second-Order Interferometry. *J. Phys. Chem. B* **2001**, *105*, 2135−2142.

(74) Nishiyama, Y.; Imaeda, K.; Imura, K.; Okamoto, H. Plasmon Dephasing in Single Gold Nanorods Observed by Ultrafast Time-Resolved near-Field Optical Microscopy. *J. Phys. Chem. C* **2015**, *119*, 16215−16222.

(75) Sun, Q.; Yu, H.; Ueno, K.; Kubo, A.; Matsuo, Y.; Misawa, H. Dissecting the Few-Femtosecond Dephasing Time of Dipole and Quadrupole Modes in Gold Nanoparticles Using Polarized Photoemission Electron Microscopy. *ACS Nano* **2016**, *10*, 3835−3842.

(76) Collins, S. S. E.; Searles, E. K.; Tauzin, L. J.; Lou, M.; Bursi, L.; Liu, Y.; Song, J.; Flatebo, C.; Baiyasi, R.; Cai, Y.-Y.; et al. Plasmon Energy Transfer in Hybrid Nanoantennas. *ACS Nano* **2021**, *15*, 9522−9530.

(77) Foerster, B.; Rutten, J.; Pham, H.; Link, S.; Sönnichsen, C. Particle Plasmons as Dipole Antennas: State Representation of Relative Observables. *J. Phys. Chem. C* **2018**, *122*, 19116−19123.

(78) Hu, M.; Novo, C.; Funston, A.; Wang, H.; Staleva, H.; Zou, S.; Mulvaney, P.; Xia, Y.; Hartland, G. V. Dark-Field Microscopy Studies of Single Metal Nanoparticles: Understanding the Factors That Influence the Linewidth of the Localized Surface Plasmon Resonance. *J. Mater. Chem.* **2008**, *18*, 1949−1960.

(79) Cushing, S. K.; Li, J.; Meng, F.; Senty, T. R.; Suri, S.; Zhi, M.; Li, M.; Bristow, A. D.; Wu, N. Photocatalytic Activity Enhanced by Plasmonic Resonant Energy Transfer from Metal to Semiconductor. *J. Am. Chem. Soc.* **2012**, *134*, 15033−15041.

(80) Li, J.; Cushing, S. K.; Meng, F.; Senty, T. R.; Bristow, A. D.; Wu, N. Plasmon-Induced Resonance Energy Transfer for Solar Energy Conversion. *Nat. Photonics* **2015**, *9*, 601−607.

(81) Zheng, Y. B.; Kiraly, B.; Cheunkar, S.; Huang, T. J.; Weiss, P. S. Incident-Angle-Modulated Molecular Plasmonic Switches: A Case of Weak Exciton-Plasmon Coupling. *Nano Lett.* **2011**, *11*, 2061−2065.

(82) Miyajima, Y.; Tison, Y.; Giusca, C. E.; Stolojan, V.; Watanabe, H.; Habuchi, H.; Henley, S. J.; Shannon, J. M.; Silva, S. R. P. Probing the Band Structure of Hydrogen-Free Amorphous Carbon and the Effect of Nitrogen Incorporation. *Carbon* **2011**, *49*, 5229−5238.

(83) Huang, X.; Li, H.; Zhang, C.; Tan, S.; Chen, Z.; Chen, L.; Lu, Z.; Wang, X.; Xiao, M. Efficient Plasmon-Hot Electron Conversion in Ag-Cspbbr3 Hybrid Nanocrystals. *Nat. Commun.* **2019**, *10*, 1163.